JTTEE5 19:950–957
DOI: 10.1007/s11666-010-9498-8
1059-9630/$19.00 © ASM International

Novel In Situ Transformable Coating for Elevated-Temperature Applications

J. Zhou, J.K. Walleser, B.E. Meacham, and D.J. Branagan

(Submitted October 1, 2009; in revised form January 4, 2010)

This article presents a new glass forming twin wire-arc thermal spray coating which is applicable to elevated temperature environments involving erosion and corrosion. When sprayed using conventional twin wire-arc spray technology, primarily amorphous coating is obtained containing an amorphous matrix with very small nanocrystalline precipitates that are less than 10 nm in size. The as-sprayed coating is found to be very hard and abrasion resistant. However, during elevated temperature exposure such as in coal-fired or biomass boiler environments, the coating may devitrify into fully nanocrystalline state consisting of α-Fe and $M_2(BC)_1$ phases. When this occurs the microhardness is found to increase dramatically by over 200 kg/mm^2 which leads to an increase in abrasion resistance by a factor of 3.5 with an analogous increase in erosion resistance. Due to the significance of these beneficial changes in coating behavior, the kinetics of the devitrification transformation was investigated using isothermal experiments and modeled with classical nucleation theory. Predictive behavior was then enabled through the development of a time-temperature-transformation diagram to model the devitrification transformation under specific thermal exposures, which was additionally confirmed by experimentation.

Keywords boiler, devitrification, erosion, kinetics, metallic glass, nanocomposite, thermal spray coating

1. Introduction

Common problems in power generation, independent on whether the boiler design is a coal-fired, oil-fired, or a municipal waste-to-energy boiler, are high temperature erosion and corrosion of boiler tubes for which the application of thermal spray coating materials to protect the tube surfaces is a general industry practice. Detailed reviews about several types of thermal spray coating can be found elsewhere (Ref 1-7). Recently, the NanoSteel Company reported a nanocomposite coating that was formed from an iron-based amorphous alloy, SHS7170, using conventional twin wire-arc thermal spraying technology (Ref 1). When heated to temperatures above its peak crystallization temperature, the as-sprayed coating containing an iron-based amorphous matrix with nanoscale carbides and borides fully devitrified into interdispersed three-phases (ferrite, carbide and boride) nanocrystals that demonstrated high performance at elevated temperature-erosion testing (Ref 1).

The SHS8000 alloy is a more recent iron-based alloy coating that was developed by the NanoSteel Company. Compared to the previous SHS7170 coating (Ref 1), it has enhanced glass forming ability, which allows the formation of a primary amorphous matrix upon initial spraying. The as-sprayed coating has been demonstrated to possess high hardness, low wear rate, and improved erosion resistance. At elevated temperatures in the application temperature ranges found in boilers, the SHS8000 coating is found to get harder and more erosion resistance which is in contrast to many other materials which are found to get worse during elevated temperature exposure (Ref 3-8).

Depending on the design of boiler systems, fuel used (coal, oil, gas, or biomass), and the tube locations in a boiler, the applied protective coating is subjected to wide temperature ranges that may span from 300 to 700 °C (Ref 3-7). Evaluating high-temperature performance and potential changes in coating properties during thermal exposure are of paramount importance to ensure long-life service and avoid unforced outages. Toward these considerations, isothermal kinetic experiments were conducted on the as-sprayed SHS8000 coating and the data were analyzed and modeled with the classical nucleation theory in order to plot a time-temperature-transformation (TTT) curve for the devitrification process and to provide predictive capability for coating performance (Ref 9), which was confirmed by experiments.

2. Experimental Procedure

The as-sprayed coating was characterized, heat treated, tested at elevated temperatures, and analyzed by means of a series of experimental approaches as presented below. Isothermal experiments were carried out at six different temperatures and a theoretical framework was then developed to explore the in situ transformation kinetics during in-service period.

J. Zhou, J.K. Walleser, B.E. Meacham, and **D.J. Branagan**, The NanoSteel Company, 505 Lindsay Boulevard, Idaho Falls, ID 83402. Contact e-mail: jzhou@nanosteelco.com.

2.1 Coating Materials, Characterization, and Heat Treatment

The SHS8000 coating is a proprietary glass forming alloy containing chromium (<22 wt.%), molybdenum (<5 wt.%), niobium (<5 wt.%), boron (<5 wt.%), carbon (<2 wt.%), manganese (<1 wt.%), silicon (<1 wt.%), with the balance iron. The coating was deposited onto 1″ by 3″ by ¼″ (25.4 by 76.2 by 6.4 mm) plain carbon steel coupons using a TAFA 8835 arc gun under optimized spray conditions that were determined experimentally. During the twin wire-arc thermal spray processes two continuously fed electrically conductive wires of ~1.6 mm in diameter served as consumable electrodes and were melted by means of an electric arc that had a current range of 220-250 A and a voltage range of 32-34 V. The molten material was atomized by high velocity compressed air at a pressure of 50-60 psi (0.35-0.41 MPa) and propelled toward the grit blasted substrate surface that was 4-6 inches (101.6-152.4 mm) away from the spray gun. The impacting molten particles on the substrate rapidly solidified to form a coating through the continuous buildup of individual splats. This arc spray process carried out correctly is called a ''cold process'' (relative to the substrate material being coated) as the substrate temperature can be kept low during processing to avoid damage, metallurgical changes and distortion to the substrate material.

After characterizing the macroscale structural features in the cross sections of the coating using an optical microscope, differential thermal analysis (DTA) was carried out in a Perkin Elmer DTA-7 system to determine the crystallization temperatures for the coating materials. The phases in the as-sprayed coating were analyzed using x-ray diffraction that was carried out in a Panalytical X'Pert MPD diffractometer with a Cu Kα x-ray tube and operated at 40 kV with a filament current of 40 mA. Scans were run with a step size of 0.01° and an integration time of 1 s from 20° to 100° 2θ.

The nanoscale structural features were examined using high resolution transmission electron microscopy (TEM). To prepare TEM samples, specimens were carefully cut, mounted, thinned, and milled until perforation using a Gatan 691 Precision Ion Polishing System. The specimens were then mounted on a single tilt stage holder and examined in a JEOL 2010 TEM. In order to understand the upper bound of structural evolution at elevated temperatures, the as-sprayed coating was heat treated at 800 °C for 2 h to obtain full devitrification phase constituents and structural features that were again examined and analyzed using x-ray diffraction and high resolution TEM.

2.2 Elevated-Temperature Erosion Testing

The potential property changes at elevated temperatures were investigated by exposing the coating in air at 600 °F (316 °C), 900 °F (482 °C), and 1200 °F (649 °C), respectively, for 20 min, during which elevated-temperature erosion testing was carried out in a laboratory scale erosion tester using fly ash from an operating circulating fluidized bed combustor boiler as the erodent material. The fly ash was applied at 3.5 g/min loading in a fixed angle of 30° with velocity of 40 m/s. The resulting scar depth was derived by laser profilometry measurement. More details on the erosion testing procedure can be found in Ref 10.

2.3 Effects of Elevated-Temperature Exposure on Microhardness and Wear Resistance

After exposure to erosion testing at three different elevated temperatures, the coating was cooled down to room temperature. Vickers microhardness measurements and wear testing were subsequently carried out to determine the resulting property changes. Microhardness testing was conducted following the protocols of ASTM E384-08 using a 100 g load. Considering the fact that thermal spray coating is not fully dense and contains small volume fractions of structural defects such as pores or microscale cracks, microhardness was also measured using a 300 g load (Ref 5, 10). Higher applied load makes bigger and deeper indents, which tends to average the pores and defects with the fully dense regions. Wear testing was conducted on a Falex Abrasion Test Machine following the ASTM G65-04 Procedure B protocol, a method commonly referred to as dry sand/rubber wheel abrasion. This test method measures the mass loss (gram) of a specimen after a fixed number of rotations of the rubber wheel at a fixed speed.

2.4 Isothermal Experiment and Kinetic Analysis

Isothermal kinetic experiments were carried out also in a Perkin Elmer DTA-7 system on the rapidly solidified alloy samples with masses of approximately 35 mg. The samples were heated at 10 °C/min to each targeting temperature in a range from 555 to 590 °C. They were then isothermally held at constant temperature until crystallization was detected, i.e., detection of an exothermic peak resulting from the release of heat of fusion. Classical nucleation theory was then applied to the data obtained from the isothermal experiments to develop predictive devitrification kinetics, which was validated by an additional isothermal experiment.

3. Results and Discussion

3.1 The As-Sprayed and Fully Devitrified Coating

The optical micrograph in Fig. 1 shows the macroscale structural features in the cross section of the as-sprayed SHS8000 coating. High coating densities, typically with porosity in the range from 2% to 5% were obtained. Note that unlike conventional coatings the microstructural features in the as-sprayed SHS8000 coating cannot be observed in SEM, due to its very fine nanoscale structure.

The DTA scan (Fig. 2) shows that the alloy has a single glass to crystallization peak with the onset at 620 °C and

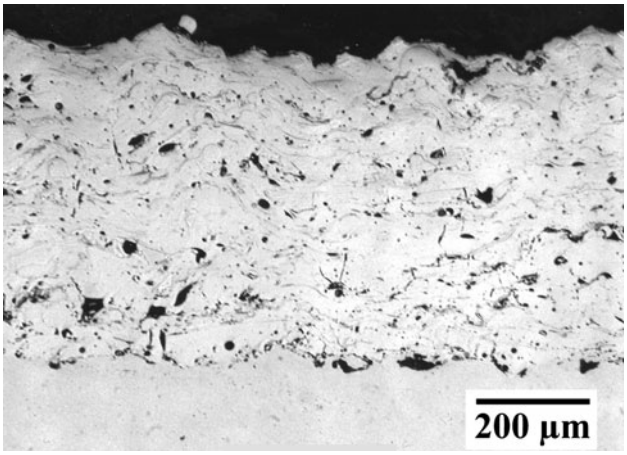

Fig. 1 Optical micrograph showing the macroscale structure features in the cross section of the as-sprayed SHS8000 coating

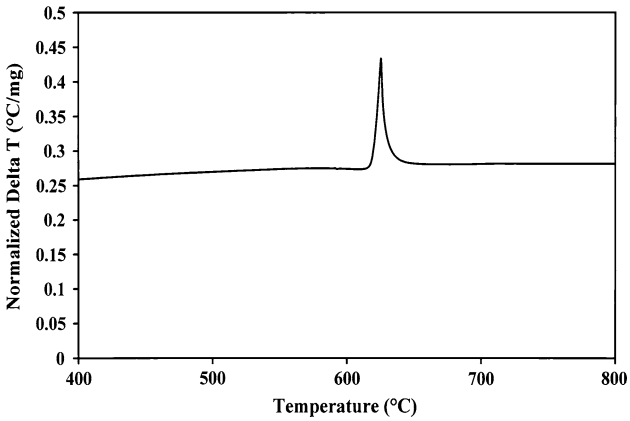

Fig. 2 DTA scan of the rapidly solidified SHS8000 alloy showing the glass to crystalline transformation

the peak temperature at 625 °C. The crystallization temperature is approximately one half of the melting temperature that is around 1201 °C. Since diffusion at the devitrification temperature is sluggish and the driving force for nucleation is high due to the metastable nature of the glass state, a very high nucleation frequency occurs with limited amount of time for grain growth before impingement, allowing for the formation of nanoscale coating structures.

High resolution x-ray diffraction analysis and TEM micrograph show that the as-sprayed coating is an amorphous metallic glass matrix composite (Fig. 3). The prevalent broad hump in the background of the x-ray diffraction spectrum (Fig. 3a) indicates that the volume fraction of the glass matrix is significant. Additionally, there are very small volume fractions of crystalline phases that were identified as α-Iron (ferrite) and $M_2(BC)_1$ where M refers to a mixture of transition metals. The nanocrystalline phases as shown by the TEM image (Fig. 3b) are less than 10 nm in size and appear as bright or dark nanocrystals in the high-resolution TEM image, due to their different crystalline orientation. Note that the electron diffraction corresponding to these tiny nanocrystals is not observable in the selected area electron diffraction (SAED) pattern (inset of Fig. 3b) since the major peaks of the nanoscale ferrite and $M_2(BC)_1$ are enclosed into the broad hump which has high diffraction intensity. The diffraction intensities of all other crystalline peaks are much weaker than the amorphous hump (Fig. 3a).

After being annealed at 800 °C for 2 h, the amorphous matrix is fully devitrified, as indicated by the lack of the amorphous background in the x-ray diffraction pattern (Fig. 3c). However, no additional diffraction peaks were identified when comparing the two x-ray diffraction spectra (Fig. 3a and c). In other words, the entire amorphous matrix devitrified into ferrite and $M_2(BC)_1$, and no other additional phases are formed in the accelerated devitrification at elevated temperatures. This is confirmed by the high resolution TEM image (Fig. 3d), which shows that the compound phase remains as tiny nanoscale grains dispersed in the ferrite matrix. The crystalline structures, space group, and lattice parameters of the phases were identified by Rietveld analysis and given in Table 1. It should be noted that the 800 °C heat treatment was chosen to ensure complete devitrification but represents an upper bound for coating thermal exposure since excessive grain growth is occurring leading to relatively coarse grains up to 200 to 500 nm. Previous studies in a similar iron-based amorphous materials showed that excessive grain growth does not occur until temperatures greater than 750 °C (Ref 8).

3.2 Elevated Temperature Erosion

The results of the elevated-temperature erosion testing are shown in Fig. 4. The maximum scar depth and the volume loss of SHS8000 coating is reported in comparison with the plain carbon steel substrates, representing uncoated heat exchange tubes that were tested under identical conditions. It is well known that all materials including protective coating is less erosion resistant as the temperature is increased and for most materials and coatings, the degradation of erosion resistance exhibits an exponential increase with temperatures (Ref 1, 5, 10). The increasing scar depth (Fig. 4a) and volume loss (Fig. 4b) with increasing testing temperature for 1018 steel substrate are consistent with this trend. At the lowest temperature of 600 °F (316 °C), the 1018 steel substrates have quite good erosion resistance; however, this is believed to be a fortuitous result from the formation of a hard thin oxide layer which was adherent during this temperature range. As the testing temperature was increased to 900 °F (482 °C), the thin protective oxide layer on the otherwise soft 1018 steel substrate fails, and the SHS8000 coating provides superior performance. At the highest testing temperature of 1200 °F (649 °C), the performance of the SHS8000 coating is even more significant and better than expected unless simultaneous changes in coating properties are occurring. The improved erosion resistance is believed to be associated with the in situ phase transformation that takes place in the coating at elevated

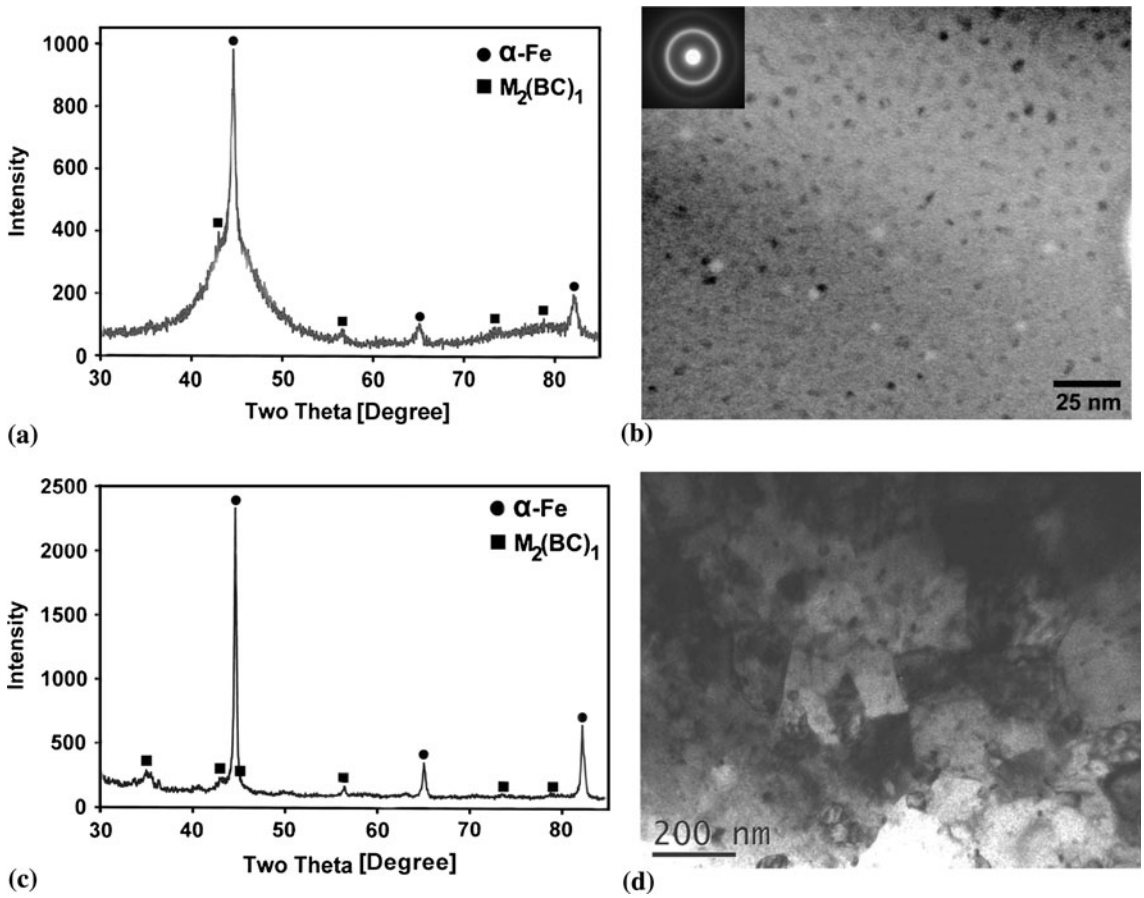

Fig. 3 Phases and nanostructures in the as-sprayed and fully devitrified SHS8000 coating: (a) x-ray diffraction and (b) TEM image of the as-sprayed coating; (c) x-ray diffraction and (d) TEM image of the fully devitrified coating after heating at 800 °C for 2 h

Table 1 Phases identified in the devitrified SHS8000 wire-arc coating

Phase	Crystal system	Space group	Lattice parameter(s), Å
α-Fe	Cubic	*Im3m*	$a = 2.871$
$M_2(BC)_1$	Tetragonal	*I4/mcm*	$a = 5.136$, $c = 4.239$

temperatures which is maximized when the testing temperature was increased to 1200 °F (649 °C) (Ref 2, 8, 9).

3.3 Property Changes Resulting from Elevated Temperature Exposure

Microhardness changes after exposure to high testing temperatures are presented in Fig. 5(a). In the as-sprayed state, the nanocomposite coating exhibits 300HV microhardness in the range of 1050-1230 kg/mm^2. When the as-sprayed coating is exposed to temperatures in the range of 600 °F (316 °C) to 900 °F (482 °C) for 20 min, there is a slight increase (Fig. 5a) in coating microhardness. Sine this temperature range is lower than the crystallization temperature (Fig. 2), crystallization-induced hardening is unlikely to occur. The slight increase in microhardness may be a result of possible structure relaxation and the release of some residual stress formed during coating fabrication. When the coating was subjected to 1200 °F (649 °C) for 20 min, the microhardness dramatically increases by ~200 kg/mm^2. The above results suggest that the coating may be subject to full devitrification during the 1200 °F (649 °C) exposure and this is consistent with the DTA data which shows that the onset of crystallization at a heating rate of 10 °C/min is 1148 °F (620 °C). It is well known that nanocrystals resulting from full devitrification usually leads to significantly increase in microhardness (Ref 2, 8, 11). At high temperature, the in situ hardening due to the in situ formed nanocrystals counteracts the softening effect caused by temperature rising, and leads to enhanced erosion resistance of the SHS8000 coating.

The coating samples show consistently improved wear resistance as the exposure temperature increases (Fig. 5b). Again the most dramatic increase in wear resistance is achieved at the highest temperature, i.e., 1200 °F (649 °C) with a reduction in abrasion rate by a factor of 3.5 over the as-sprayed value. Interestingly, smaller but still significant abrasion resistance improvements were obtained for the coating that was exposed to the two lower temperatures, 600 °F (316 °C) and 900 °F (482 °C), respectively (Fig. 5b). This may be due to recovery and relaxation

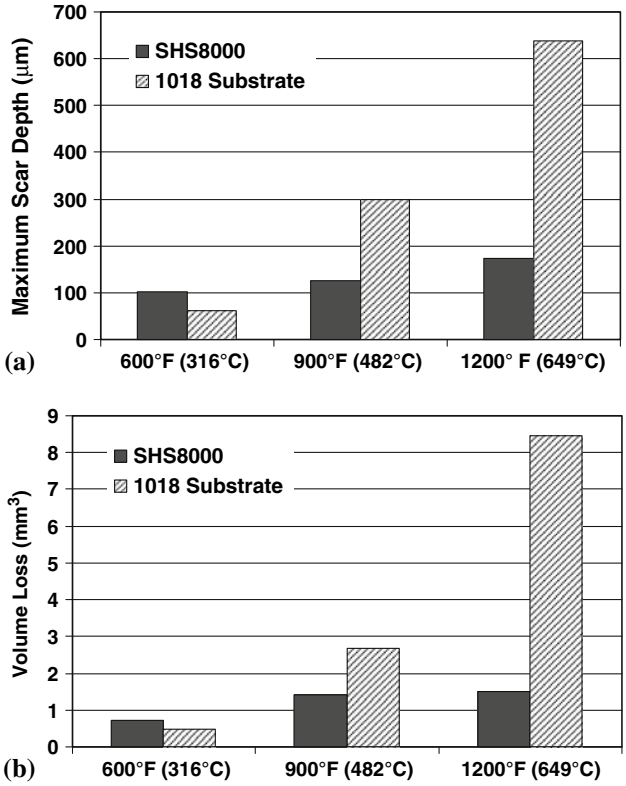

Fig. 4 In situ improved erosion resistance at elevated temperatures: (a) the maximum scar depth and (b) the erosion volume loss

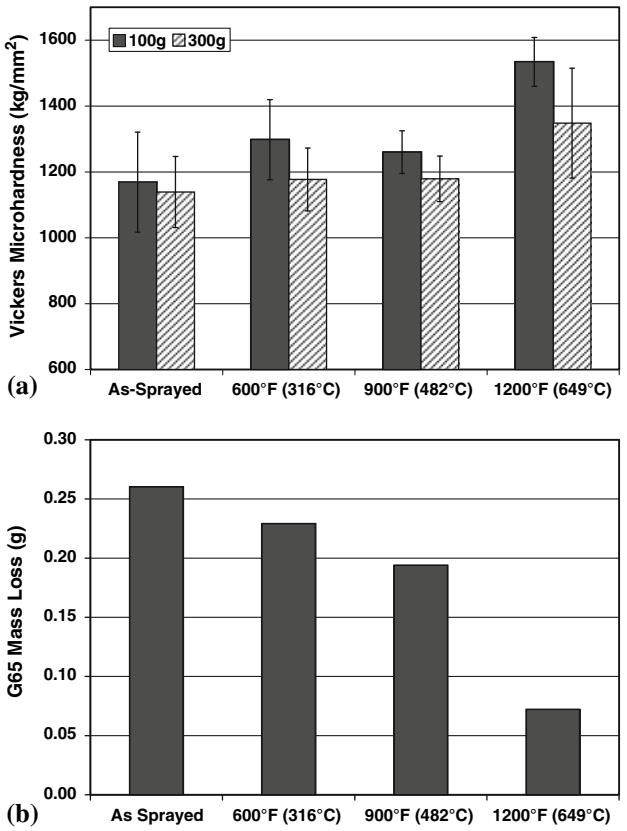

Fig. 5 Coating property improvements resulting from exposure to elevated temperatures: (a) increase in microhardness and (b) wear resistance improvement

effects occurring in the metallic glass matrix, as documented previously in iron-based metallic glasses when heat treated at temperatures far below the crystallization temperature (Ref 11).

3.4 Isothermal Experiments and Kinetics Analysis

In Fig. 6, the temperature history of an isothermal experiment performed at 570 °C is shown, where both the heating and holding stages are indicated. On the heat flow spectrum, the tangential lines of the background and the crystallization peak were, respectively, drawn to get the crossing point, which is defined as the onset of crystallization. In order to obtain the thermodynamic parameters, the results of six isothermal experiments were fitted to a kinetic equation. Subsequently, an additional isothermal experiment was performed to evaluate the kinetic prediction at a relatively low temperature (540 °C) following the same isothermal experimental procedure.

Representative isothermal scans are shown in Fig. 7 for several application temperatures. As the temperature decreases, it takes longer time for crystallization and the peaks become smaller and broader reflecting the impact of other processes such as glass relaxation. The results of the isothermal experiments are presented by plotting the natural log of the onset time of crystallization at various temperatures versus the inverse of temperature (Fig. 8).

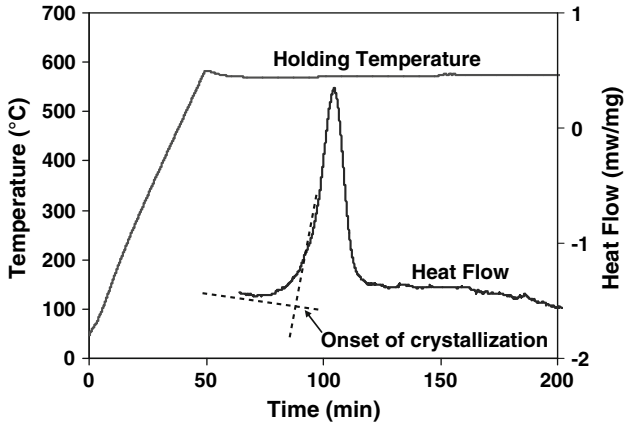

Fig. 6 Temperature profile at 570 °C is shown as a representative of isothermal kinetic experiments and determination of onset of crystallization is also indicated in the heat flow scan

Using the least squares fitting method, the data can be best fitted into a linear equation in the form:

$$\ln t = -43.134 + 40352\frac{1}{T} \quad \text{(Eq 1)}$$

where t is the onset time of crystallization detected by DTA and T is the temperature in Kelvin.

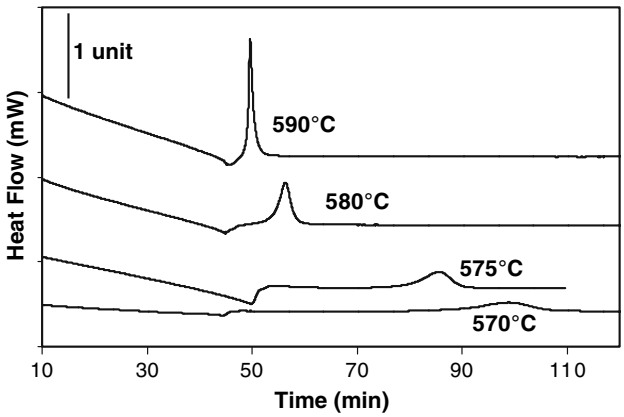

Fig. 7 Isothermal scans as a function of time for different temperatures show the amount of time until crystallization occurs as an exothermic peak

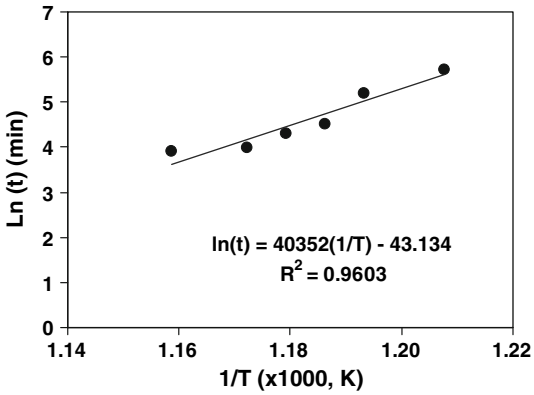

Fig. 8 The results of isothermal kinetic experiment and the best linear fitting

According to a previous study on the crystallization of amorphous metals (Ref 12), the measured temperature-time-transformation (TTT) diagram can be successfully fitted using the following crystal nucleation rate (I_v) and growth rate (u):

$$I_v = A_\upsilon D_{\text{eff}} \exp\left(\frac{-16\pi\gamma^3}{3k_B T(\Delta G)^2}\right) \quad \text{(Eq 2)}$$

$$u = \frac{D_{\text{eff}}}{a}\left[1 - \exp\left(\frac{-v\Delta G}{k_B T}\right)\right] \quad \text{(Eq 3)}$$

where A_υ is a fitting parameter, γ is the interfacial energy per area for the interface between crystalline and amorphous phases, a is the average atomic diameter, v is the average atomic volume, k_B is the Boltzman constant, and ΔG is the Gibbs free energy per volume difference between the amorphous and crystalline phases. At low temperatures, appropriate in this study, the effective diffusivity (D_{eff}) is best described by an Arrhenius law, i.e., $D_{\text{eff}} = D_0 \exp(-E_d/k_B T)$ with E_d as the activation energy and D_0 as the pre-exponent constant. Note that nucleation at the initial stage is fast and the nucleated nanocrystals do not impinge on one another. For three-dimensional particle growth the crystallization time corresponding to an instrument detectable volume fraction (f_c) is (Ref 13):

$$t = \left(\frac{3f_c}{\pi I_v u^3}\right)^{\frac{1}{4}} \quad \text{(Eq 4)}$$

Inserting Eq 2 and 3 to Eq 4 and taking the necessary approximation as $v\Delta G \ll k_B T$, we get:

$$\ln t = \Gamma' + \frac{1}{T}\left(\frac{4\pi\gamma 3}{3k_B(\Delta G)^2} + \frac{E_d}{k_B}\right) + \frac{3}{4}\ln\left(\frac{v\Delta G}{k_B T}\right) \quad \text{(Eq 5)}$$

where Γ' includes all temperature-independent factors and is simply a fitting constant. E_d has a constant value, and γ and ΔG are temperature-dependent parameters to be determined. Torrens-Serra et al. (Ref 14) showed that the interfacial energy and the Gibbs free energy difference for iron-based metallic glasses are:

$$\gamma = 577.0 - 54.56T\,(\text{mJ/m}^2) \quad \text{(Eq 6)}$$

$$\Delta G = 123746 - 12.6T\,(\text{J/mol}) \quad \text{(Eq 7)}$$

Since the SHS8000 alloy in this study is a new alloy system, no particular expressions have been developed or identified for it but the alloy composition is close enough to the alloy studied by Torrens-Serra et al., so Eq 6 and 7 may be used to facilitate our kinetic study.

In the temperature range from 440 to 620 °C, the last term on the right side of Eq 5 is close to a constant value of 5. For approximation, it may be treated as a constant and enclosed into Γ'. Equation 5 is, therefore, reduced to a simpler format:

$$\ln t = \Gamma + \frac{1}{T}\left(\frac{4\pi\gamma 3}{3k_B(\Delta G)^2} + \frac{E_d}{k_B}\right) \quad \text{(Eq 8)}$$

Inserting Eq 6 and 7 to Eq 8 and comparing it with the fitting Eq 1, the activation energy of diffusion is able to be calculated. For the SHS8000 alloy, it is 3.48 eV, which is a value close to 4.37 eV obtained by Torrens-Serra et al. (Ref 14). In fact, the value of the first term in the bracket of Eq 7 is on the order of 10^{-6} K, which is small when compared to 40352 K obtained by linear fitting of the isothermal experiment data (Eq 1). In other words, the activation energy of diffusion can be accurately obtained by fitting the experimental data.

Using Eq 8, we are able to calculate the onset time for crystallization and the low-temperature part of the TTT diagram is accordingly formed and shown in Fig. 9, in which the experimental data are also included for comparison. As shown, while devitrification occurs very quickly at elevated temperatures greater than ~700 °C, devitrification does not initiate until a 1 year thermal exposure at 443 °C. Additionally, according to the calculation, the onset of crystallization at 540 °C can be predicted to occur at 664 min. The prediction is proved to be valid by the additional isothermal experiment, in which the DTA detected the onset of crystallization at 660 min.

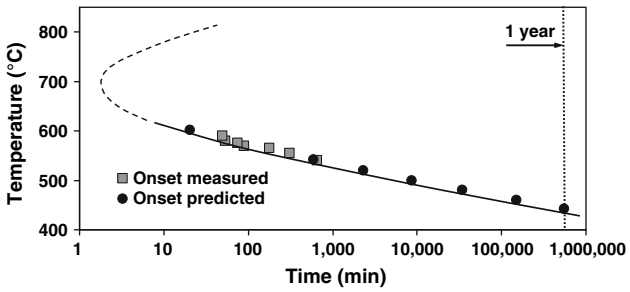

Fig. 9 Experiment-based calculation of crystallization TTT diagram for the metallic glass coating is plotted in comparison with the results of the isothermal kinetic experiments

The close match-up between the predicted and measured onset times suggests that the experiment-based kinetic calculation is accurate, at least for the temperature range of our interest in operating power plants. Moreover, such a calculation is very important to understand the crystallization behavior of the amorphous coating over long-term service at elevated temperatures.

It should be noted that a similar linear kinetic equation was obtained using the classical nucleation and growth theory for a Zr-based glass coating (Ref 15). This further confirms that the calculated crystallization kinetics (Fig. 9) is valid and reasonably accurate. This is true at least for the low temperature regime, i.e., the temperatures below the nose of the ''C'' shaped TTT curve. At high temperature regime, the diffusivity may obey a Stokes-Einstein relationship and is a function of the viscosity, which in turn is temperature dependent. Considering this, the upper portion of the TTT curve is schematically illustrated using a dashed curve. Since temperature range in which the coating services is relatively low, crystallization kinetics at high temperature regime is beyond the focus of this work. At the highest studied temperature, 1200 °F (649 °C), microhardness significantly increases by ~200 kg/mm^2, leading to dramatic improvement in wearing resistance by a factor of 3.5. According to the kinetic prediction, devitrification occurs at ~600 °C to occur within ~20 min. At 649 °C, full devitrification can be reasonably expected within 20 min of exposure time.

4. Conclusions

The SHS8000 coating is an iron-based glass forming alloy with a low critical cooling rate for metallic glass formation appropriate for thermal spray deposition. Upon spraying using conventional twin wire-arc spray technology, it forms primarily amorphous coating containing an amorphous matrix with very fine dispersed nanocrystals that were identified as ferrites and $M_2(C,B)_1$ compounds. When exposed to elevated temperatures, the microhardness slightly increased at relatively low temperatures from 600 °F (316 °C) to 900 °F (482 °C), and the microhardness dramatically increases up to ~200 kg/mm^2 when the temperature was raised to 1200 °F (649 °C). Corresponding to the significant hardening, the wear resistance was improved by a factor of 3.5 and similar improvement was also obtained for elevated-temperature erosion resistance.

The isothermal experiments and kinetic prediction show that crystallization is slow at low temperatures but full devitrification occurs well within 20 min at 1200 °F (649 °C), the highest exposure temperature. The dispersed nanoscale $M_2(BC)_1$ compounds and the overall nanoscale grain structure formed by in situ devitrification are believed to be the two main causes for performance improvement of the coating at elevated temperatures. The development of the TTT diagram for the SHS8000 coating allows for predictive capability to determine coating performance as a function of temperature and time during elevated temperature exposure.

Acknowledgments

The authors thank Dr. J.E. Shield and Mr. B. Merkle for insightful discussion and help with microstructure analysis and thermal spray sample preparation.

References

1. D.J. Branagan, M. Breitsameter, B.E. Meacham, and V. Belashchenko, High-Performance Nanoscale Composite Coatings for Boiler Applications, *J. Therm. Spray Tech.*, 2005, **14**, p 196-204
2. J. Branagan and Y. Tang, Developing Extreme Hardness (>15 GPa) in Iron Based Nanocomposites, *J. Compos. A*, 2002, **33**, p 855-859
3. S.H. Lee, N.J. Themelis, and M.J. Castaldi, High-Temperature Corrosion in Waste-to-Energy Boilers, *J. Therm. Spray Tech.*, 2007, **16**, p 104-110
4. K. Tani and Y. Harada, Enhancement of Service Life of Steam Generating Tubes in Oil-Fired Boiler for Power Generation Employing Plasma Spray Technology, *J. Therm. Spray Tech.*, 2007, **16**, p 111-117
5. D.J. Branagan, W.D. Swank, and B.E. Meacham, Maximizing the Glass Fraction in Iron Based HVOF Coatings, *Metall. Mater. Trans. A*, 2009, **60**, p 1306-1313
6. Y. Matsubara, Y. Sochi, M. Tanabe, and A. Takeya, Advance Coating on Furnace Wall Tubes, *J. Therm. Spray Tech.*, 2007, **16**, p 195-201
7. Y. Kawahara, Application of High Temperature Corrosion-Resistant Materials and Coatings Under Severe Corrosive Environment in Waste-to-Energy Boilers, *J. Therm. Spray Tech.*, 2007, **16**, p 202-213
8. D.J. Branagan, Engineering Structure on a Nanoscale Level to Achieve Targeted Properties in Steels, *CALPHAD*, 2007, **31**, p 343-350
9. L. Kaufman, J.H. Perepezko, K. Hildal, J. Farmer, D. Day, N. Yang, and D.J. Branagan, Transformation, Stability and Pourbaix Diagrams of High Performance Corrosion Resistant (HPCRM) Alloys, *CALPHAD*, 2009, **33**, p 89-99
10. D.J. Branagan, M.C. Marshall, and B.E. Meacham, Formation of Nanoscale Composite Coatings Via HVOF and Wire-Arc Spraying, *Proceedings of the ITSC 2005*, May 2-4, 2005 (Basel, Switzerland), p 539-544
11. B.B. Kappes, B.E. Meacham, Y.L. Tang, and D.J. Branagan, Relaxation, Recovery, Crystallization, and Recrystallization Transformations in an Iron-Based Amorphous Precursor, *Nanotechnology*, 2003, **14**, p 1228-1234
12. D. Xu and W.L. Johnson, Crystallization Kinetics and Glass-Forming Ability of Bulk Metallic Glasses $Pd_{40}Cu_{30}Ni_{10}P_{20}$ and $Zr_{41.2}Ti_{13.8}Cu_{12.5}Ni_{10}Be_{22.5}$ from Classical Theory, *Phys. Rev. B*, 2006, **74**, p 024207

13. D.A. Porter and K.E. Easterling, *Phase Transformations in Metals and Alloys*, 2nd ed., Stanley Thornes, UK, 1991
14. J. Torrens-Serra, J. Rodríguez-Viejo, and M.T. Clavaguera-Mora, Nanocrystallization Kinetics and Glass Forming Ability of the $Fe_{65}Nb_{10}B_{25}$ Metallic Alloy, *Phys. Rev. B*, 2007, **76**, p 214111
15. H. Hildal and J.H. Perepezko, Assessing the Thermal Stability of Bulk Metallic Glasses for Nuclear Waster Applications, *Materials Science and Technology*, J.C. Farmer, P.E.A. Turchi, and J.H. Perepezko, Ed., Curran Associate, Inc., West Chester, OH, 2007, p 361-369